Nano Research

Open Access

Research Article

Low-temperature synthesis of medium-entropy spinel oxide powders with electromagnetic wave-absorbing and anti-corrosion properties

Dandan Ma[1,2,3], Suhang Cao[1], Junjie Qian[1] ✉, Yongqing Wang[1] ✉, Mingmin Bai[1], Huanhuan Guo[1], Chi Yu[1], and Xiaozhen Zhang[1]

[1] School of Materials Science and Engineering, Jingdezhen Ceramic University, Jingdezhen 333403, China
[2] School of Materials Science and Engineering, Sichuan University of Science & Engineering, Zigong 643000, China
[3] Material Corrosion and Protection Key Laboratory of Sichuan province, Zigong 643000, China

Cite this article: *Nano Research*, **2026**, *19*, 94908562. https://doi.org/10.26599/NR.2026.94908562

ABSTRACT: To meet the requirements for electromagnetic wave (EMW) absorbing materials in corrosive environments such as the ocean, $(NiZnCuMn)Co_2O_4$ medium-entropy oxides (MEOs) with anticorrosion properties have been developed as novel EMW absorbing materials. The $(NiZnCuMn)Co_2O_4$ MEOs, which are synthesized via a hydrothermal reaction followed by calcination, exhibit robust EMW absorption performance with a minimum reflection loss of −64.05 dB and an ultrabroad effective absorption bandwidth that can reach 7.35 GHz by adjusting the hydrothermal reaction time. This high performance is attributed to the synergistic effect of dielectric loss, magnetic loss, and the unique structure of the MEOs. $(NiZnCuMn)Co_2O_4$ can be doped into epoxy resin, endowing it with excellent anti-corrosion properties. After being soaked in 3.5 wt.% NaCl for 14 days, $(NiZnCuMn)Co_2O_4$ prepared with a hydrothermal time of 12 h, shows a minimum corrosion current of 6.61×10^{-6} A/cm^2. When the hydrothermal time is 18 h, the corrosion current is 6.66×10^{-6} A/cm^2 and the corrosion potential reaches −0.712 V. This study provides new insights into the design of EMW absorbing materials with anticorrosion properties.

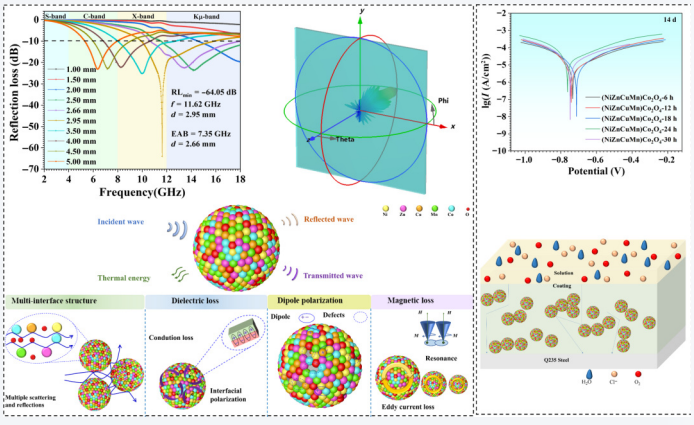

KEYWORDS: medium-entropy spinel oxides, low-temperature synthesis, microwave absorption, anti-corrosion

1 Introduction

The rapid development of radar detection technologies has sparked interest in electromagnetic wave (EMW) absorbing materials for information security and the survivability of military weapons [1, 2]. To date, various EMW absorbing materials, including conductive polymers [3–6], dielectric loss materials [7–9], and magnetic loss-materials [10–12], have been developed. However, owing to the high humidity and salt spray conditions in the marine environment, EMW absorbing coating used on equipment must also exhibit anti-corrosion performance. Therefore, multifunctional materials with excellent anti-corrosion properties and EMW absorption performance are essential [13–15].

The unique lattice distortion effect and synergistic enhancement effect of medium-high entropy ceramics endow them with potential for application in the field of radar absorption. Medium-high entropy ceramics are solid solutions formed by 3–5 or more elements [16], such as carbides [17, 18], nitrides [19, 20], borides [21, 22], and oxides [23, 24]. Traditional synthesis methods include solid-phase sintering [25], chemical solution deposition [26], and solution combustion [27]. For example, Du et al. [28] successfully fabricated the $(Hf_{0.25}Zr_{0.25}Nb_{0.25}Ta_{0.25})C$ ceramic using solid-phase sintering at 2200 °C and investigated its EMW absorption performance, finding that the minimum reflection loss (RL_{min}) reached −64.38 dB. More recently, they reported the $(Hf_{0.25}Zr_{0.25}Ta_{0.25}Nb_{0.25})C$–SiC biphasic ceramic using a polymer-derived ceramics (PDC) route at only 1500 °C. This biphasic ceramic exhibited excellent EMW absorption performance via the

Received: December 25, 2025; **Revised:** February 4, 2026
Accepted: February 11, 2026

✉Address correspondence to Junjie Qian, qianjunjie@jcu.edu.cn; Yongqing Wang, wyq8248@126.com

synergistic interaction of the $(Hf_{0.25}Zr_{0.25}Ta_{0.25}Nb_{0.25})C$ and SiC phases, with an RL_{min} of −54.28 dB. Gu et al. [29] synthesized diborides and analyzed the influence of lattice distortion on the EMW absorption performance, concluding that chemical nanoclusters and metal vacancies can improve the EMW attenuation capacity. Li et al. [30] fabricated a perovskite oxide via a wet chemical method combined with heat treatment at 1350 °C. The obtained $Sr(Cr_{0.2}Mn_{0.2}Fe_{0.2}Co_{0.2}Ni_{0.2})O_3$ material exhibited a remarkable RL_{min} of −54 dB, owing to the synergistic effect of oxygen vacancies and lattice distortion. Despite exhibiting strong EMW absorption properties, these ceramics require an extremely high synthesis temperature (above 1000 °C), and their effective absorption bandwidth (EAB) needs to be further enhanced.

In this work, novel $(NiZnCuMn)Co_2O_4$ medium-entropy oxides (MEOs) were fabricated using a simple hydrothermal reaction combined with heat treatment under moderate conditions (400 °C). The phase composition and microstructures, EMW absorption performance, and anti-corrosion properties were systematically investigated. The results indicate that the obtained urchin-shaped MEOs microspheres exhibit excellent EMW absorption performance with an RL_{min} of −64.05 dB and an EAB that can reach 7.35 GHz by adjusting the hydrothermal reaction time. Owing to their excellent anti-corrosion performance, the $(NiZnCuMn)Co_2O_4$ MEOs have potential applications in marine environments.

2 Experimental section

2.1 Materials

Nickel nitrate, cobalt nitrate, copper nitrate, liquid manganese nitrate (50 wt.%), zinc nitrate, and urea were purchased from Sinopharm Group Chemical Reagent Co., LTD. (Shanghai, China). All reagents were used without further purification.

2.2 Fabrication of $(NiZnCuMn)Co_2O_4$

$(NiZnCuMn)Co_2O_4$ powders were prepared through a simple hydrothermal reaction followed by calcination in air. In a typical experiment, 0.3635 g of $Ni(NO_3)_2{\cdot}6H_2O$, 0.3719 g of $Zn(NO_3)_2{\cdot}6H_2O$, 0.302 g of $Cu(NO_3)_2{\cdot}6H_2O$, 0.4474 g of $Mn(NO_3)_2$ (50 wt.%) solution, 2.9105 g of $Co(NO_3)_2{\cdot}6H_2O$, and 3.0030 g of $CO(NH_2)_2$ were weighed and then added to 50 mL of deionised water under magnetic stirring. The solution was poured into a Teflon container (100 mL), which was subsequently placed in a stainless-steel reactor at 105 °C for 6, 12, 18, 24, and 30 h, yielding $(NiZnCuMn)Co_2O_4$ precursors. The $(NiZnCuMn)Co_2O_4$ precursors were washed three times with deionized water and anhydrous ethanol separately, then dried in an oven at 80 °C for 24 h. The obtained materials were annealed at 400 °C (5 °C/min) in an air environment for 2 h, labelled as $(NiZnCuMn)Co_2O_4$-6 h, $(NiZnCuMn)Co_2O_4$-12 h, $(NiZnCuMn)Co_2O_4$-18 h, $(NiZnCuMn)Co_2O_4$-24 h, and $(NiZnCuMn)Co_2O_4$-30 h, respectively.

2.3 Characterization

The crystal phases of the as-obtained $(NiZnCuMn)Co_2O_4$ materials were characterised using X-ray diffraction (XRD, DX-2700B, China) (Cu Kα radiation, scan rate 2 °/min, 10°–80 °). The chemical binding states and surface elemental compositions of the as-obtained $(NiZnCuMn)Co_2O_4$ materials were recorded via X-ray photoelectron spectroscopy (XPS, Thermo K-Alpha, USA). The thermogravimetry (TG, Netzsch STA449F5, Germany) performance was recorded by a thermal gravimetric analyser in an air atmosphere (1200 °C, 10 °C/min). The mass percentage of elements were investigated using inductively coupled plasma optical emission spectrometry/mass spectrometry (ICP-OES/MS, Agilent 5110, USA). The morphologies and microstructures of the $(NiZnCuMn)Co_2O_4$ materials were investigated using scanning electron microscopy (SEM, thermo scientific Apreo 2C, UK) and transmission electron microscopy (TEM, FEI Tecnai F20, USA). The static magnetic properties of the $(NiZnCuMn)Co_2O_4$ were measured on a vibrating sample magnetometer from −2 to 2 T (VSM, LakeShore PPMS-9, USA). The relative complex permittivity and permeability of the $(NiZnCuMn)Co_2O_4$ were recorded by a vector network analyzer (VNA, KAA1171135, China).

2.4 Corrosion resistance and microwave absorption performance

The basis for evaluating the anti-corrosion performance is ASTM G106-22. The open circuit potential test (OCP), electrochemical impedance spectroscopy (EIS), and Tafel plots of the samples were measured on an electrochemical workstation (CHI660E, China). A three-electrode testing system was used, which Ag/AgCl was used as the reference electrode, a platinum sheet was used as the counter electrode and 3.5 wt.% NaCl solution was used as the electrolyte at room temperature, separately. The working electrode was formed by doping 5 wt.% $(NiZnCuMn)Co_2O_4$ powders with EP and coating them on an iron sheet. The Tafel plot was measured from −0.4 to 0.4 V vs. OCP. EIS was employed to evaluate the corrosion mitigation performance. The amplitude was 10 mV and the frequency range was 0.01–100,000 Hz.

The powder samples were mixed with paraffin at a mass ratio of 1:1, and then the mixture was pressed into a circular ring with the outer diameter of 7 mm, the inner diameter of 3.04 mm, and the thickness of 2–3 mm. The electromagnetic parameters were tested within the frequency range of 2–18 GHz. The reflection loss (RL) values of materials at corresponding frequencies with different thicknesses were calculated by using relevant parameters.

RL is derived based on the transmission line theory and it is an important indicator used to evaluate the microwave absorption performance of materials. The calculation formula for RL is [7]

$$RL\,(dB) = 20\lg\left|\frac{Z_{in}-Z_0}{Z_{in}-Z_0}\right| \tag{1}$$

$$Z_{in} = Z_0\sqrt{\frac{\mu_r}{\varepsilon_r}}\tanh\left(j\frac{2\pi fd}{c}\sqrt{\mu_r\varepsilon_r}\right) \tag{2}$$

where Z_{in} and Z_0 represent the input impedance and free-space impedance of the prepared sample, respectively. d denotes the thickness of the sample, while c and f represent the propagation speed and frequency of the electromagnetic wave, respectively.

2.5 CST Simulation

The comprehensive numerical analysis was performed by CST studio suite software to characterize the radar cross-section (RCS). In this calculation, the dimensions (length × width × thickness) of perfect electric conductor (PEC) and $(NiZnCuMn)Co_2O_4$ were 180 mm × 180 mm × 1 mm and 180 mm × 180 mm × 2.95 mm, respectively. The $(NiZnCuMn)Co_2O_4$ were coated onto PEC plate. The monitoring frequency was 11.62 GHz. The signal attenuation

was quantitatively evaluated by comparing the peak values between the coated and uncoated configurations.

2.6 Three-layer structure simulation

To broaden the EAB of the (NiZnCuMn)Co_2O_4 MEOs, a three-layer gradient structure was designed. A first coating of (NiZnCuMn)Co_2O_4-6 h with a lower dielectric constant provided better impedance matching but poor attenuation capacity, facilitating the penetration of EMWs. The second and third coatings with moderate dielectric constants ((NiZnCuMn)Co_2O_4-18 h and (NiZnCuMn)Co_2O_4-24 h) exhibited a considerably stronger EMW absorption capacity. Iterative calculations were conducted on the three-layer material using Eq. (3) as follows

$$Z_n = \eta_n \frac{Z_{n+1} + \eta_n \tanh(\gamma_n d_n)}{\eta_n + Z_{n+1} \tanh(\gamma_n d_n)} \quad (3)$$

where η_n, γ_n, and d_n represent the intrinsic impedance, the complex propagation constant, and the thickness of the nth layer, respectively. The parameters were calculated using Eqs. (4) and (5) as follows

$$\eta_n = \eta_0 \sqrt{\frac{u_{rn}}{\varepsilon_{rn}}} \quad (4)$$

$$\gamma_r = \frac{j2\pi f}{c} \sqrt{\mu_{rn}\varepsilon_{rn}} \quad (5)$$

where η_0, μ_{rn}, and ε_{rn} represent the intrinsic impedance of air ($\eta_0 = 1$), the relative complex permeability, and the relative complex permittivity of the nth layer, respectively. The Z_n value was determined using Eqs. (3)–(5), and the RL value was calculated using Eq. (1).

3 Results and discussion

A schematic diagram of the synthesis of the (NiZnCuMn)Co_2O_4 MEOs is shown in Fig. 1. After nucleation, nitrate nuclei aggregate. Then, metal atoms self-assemble to form spheres. Finally, the hybrid nanospheres are pyrolyzed in air to produce spherical (NiZnCuMn)Co_2O_4 MEOs.

The XRD patterns of (NiZnCuMn)Co_2O_4 MEOs prepared with different hydrothermal times are presented in Fig. 2(a), and the XRD pattern of (NiZnCuMn)Co_2O_4-18 h is shown in Fig. 2(b). All the patterns exhibit diffraction peaks of spinel-structured cobaltates. As shown in Fig. 2(b), the peaks appearing within the 2θ range of 10°–80° can be assigned to the (111), (220), (311), (222), (400), (422), (511), (440), and (533) crystal planes of the standard cards of $CuCo_2O_4$ (PDF: #01-1155), $MnCo_2O_4$ (PDF: #23-1237), $ZnCo_2O_4$ (PDF: #23-1390), and $NiCo_2O_4$ (PDF: #20-0781). No diffraction peaks for impurities are observed, indicating that the materials were single-phase spinel-structured solid solutions.

The thermogravimetry and differential thermogravimetry curves of the (NiZnCuMn)Co_2O_4-18 h precursor in air are shown in Fig. 2(c), and those of the (NiZnCuMn)Co_2O_4-6 h, (NiZnCuMn)Co_2O_4-12 h, (NiZnCuMn)Co_2O_4-24 h, and (NiZnCuMn)Co_2O_4-30 h precursors in air are shown in Fig. S1 in the Electronic Supplementary Material (ESM). The first weight loss, which occurred over a temperature range from room temperature to 200 °C, can be attributed to the evaporation of water adsorbed by the (NiZnCuMn)Co_2O_4 precursor. The second weight loss (200–400 °C) is related to the water produced during the transformation of the precursor into cobaltate. The stability of the curve from 400 to 800 °C revealed that no further reaction occurred.

The BET results (Figs. 2(d) and 2(e)) indicate that all the (NiZnCuMn)Co_2O_4 MEOs exhibited typical IV-type isotherm curves, indicating the presence of a mesoporous structure. The BET surface areas of (NiZnCuMn)Co_2O_4-6 h, (NiZnCuMn)Co_2O_4-12 h, (NiZnCuMn)Co_2O_4-18 h, (NiZnCuMn)Co_2O_4-24 h, and (NiZnCuMn)Co_2O_4-30 h were determined to be 21.93, 66.77, 24.77, 67.60, and 67.47 m^2/g, respectively, and their average pore diameters were 10.75, 14.62, 14.16, 9.83, and 11.16 nm. The porous structure is conducive to dissipating EMW energy, thereby facilitating the penetration of EMWs into the material and preventing their reflection at the surface.

X-ray photoelectron spectroscopy was used to investigate the elemental composition of the (NiZnCuMn)Co_2O_4 MEOs, as shown in Figs. 2(f) and 2(g) and Fig. S2 in the ESM. The characteristic peaks of Ni 2p, Zn 2p, Cu 2p, Mn 2p, Co 2p, O 1s, and C 1s were observed, indicating the presence of Ni, Zn, Cu, Mn, Co, O, and C in the MEOs. As illustrated in Fig. 2(g), the O 1s spectrum displayed three peaks at binding energies of 529.5 eV (OI), 531.3 eV (OII), and 532.4 eV (OIII). The OI peak is related to the lattice oxygen in metal–oxygen bonds. The OII peak indicates the formation of oxygen vacancies, providing defect sites to attenuate EMWs via defect polarization. The OIII peak can be attributed to surface-adsorbed water. The Rietveld XRD refinement confirms that the lattice constants of (NiZnCuMn)Co_2O_4-6 h, (NiZnCuMn)Co_2O_4-12 h, (NiZnCuMn)Co_2O_4-18 h, (NiZnCuMn)Co_2O_4-24 h, and (NiZnCuMn)Co_2O_4-30 h are 8.115, 8.122, 8.119, 8.123, and 8.123 Å, respectively (Fig. S2 in the ESM).

In the high-resolution Ni 2p spectrum (Fig. S3(a) in the ESM), the spin–orbit peaks with binding energies of 855.4 and 872.1 eV correspond to Ni $2p_{3/2}$ and Ni $2p_{1/2}$, respectively. After Gaussian fitting, the Ni $2p_{1/2}$ peak split into two peaks belonging to Ni^{3+} (872.2 eV) and Ni^{2+} (868.1 eV). Similarly, the Ni $2p_{3/2}$ peak was deconvoluted into Ni^{3+} (855.5 eV) and Ni^{2+} (854.0 eV) peaks. The two apparent peaks at binding energies of 1043.7 and 1020.8 eV

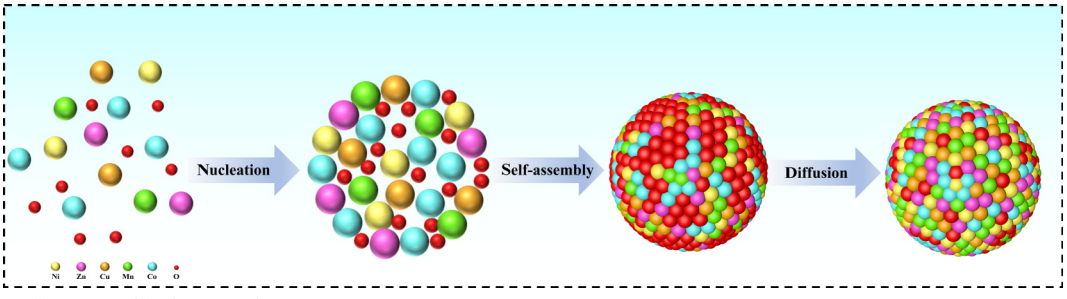

Figure 1 Schematic illustration of the formation for (NiZnCuMn)Co_2O_4.

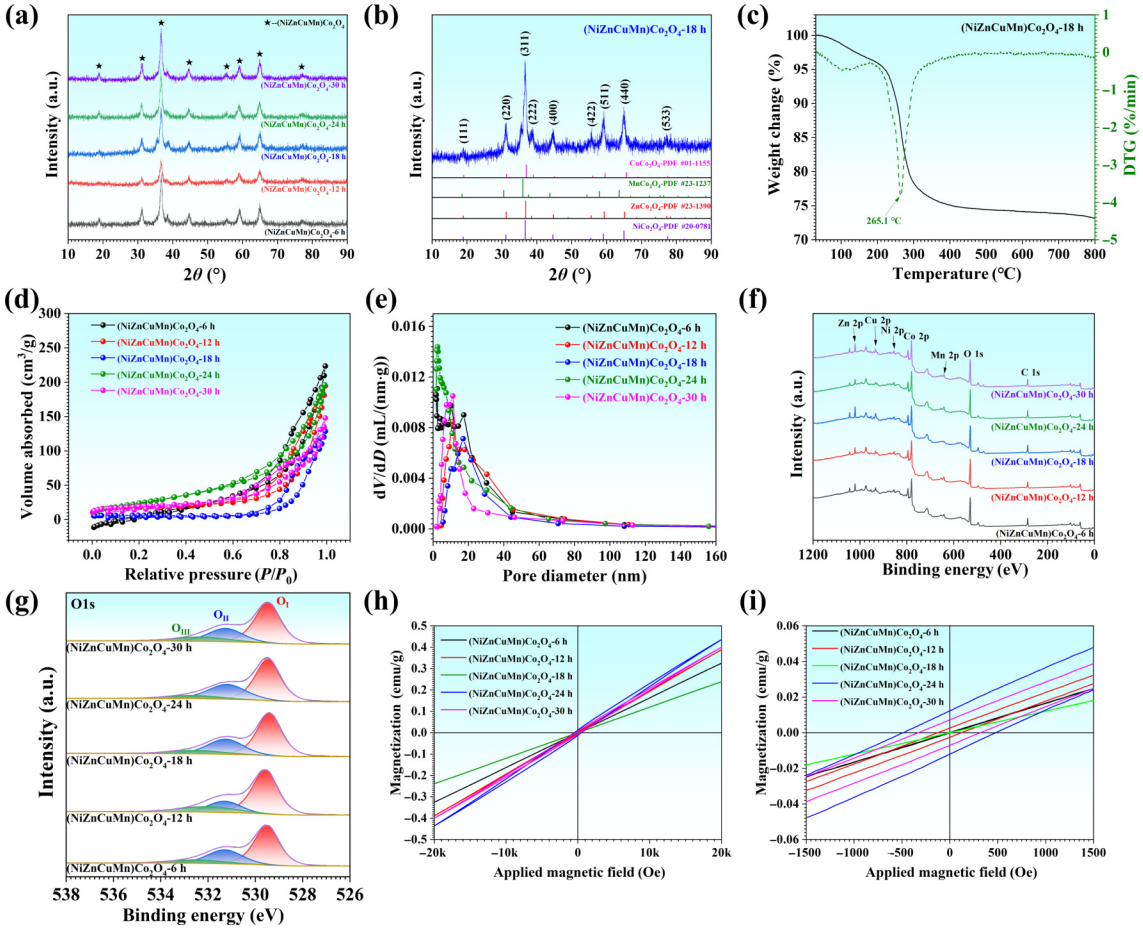

Figure 2 (a) XRD patterns of (NiZnCuMn)Co_2O_4 with different hydrothermal time. (b) XRD of (NiZnCuMn)Co_2O_4-18 h. (c) The TG and DTG curves of (NiZnCuMn)Co_2O_4-18 h precursor in air atmosphere. (d) N_2 adsorption–desorption isotherms, (e) pore size distributions, (f) XPS survey spectra, (g) O 1s, (h) hysteresis loop at room temperature (*M*–*H*), and (i) detail enlargement drawing of hysteresis loop at room temperature (*M*–*H*) for (NiZnCuMn)Co_2O_4-6 h, (NiZnCuMn)Co_2O_4-12 h, (NiZnCuMn)Co_2O_4-18 h, (NiZnCuMn)Co_2O_4-24 h, and (NiZnCuMn)Co_2O_4-30 h.

correspond to Zn $2p_{1/2}$ and Zn $2p_{3/2}$, respectively (Fig. S3(b) in the ESM). Their spin-energy separation (ΔE) is about 22.9 eV, proving that the valence state of the Zn atom was +2. In the high-resolution Cu 2p spectrum (Fig. S3(c) in the ESM), the spin–orbit peaks at 933.0 and 952.8 eV correspond to Cu $2p_{3/2}$ and Cu $2p_{1/2}$, respectively. After Gaussian fitting, the Cu $2p_{1/2}$ peak split into two components belonging to Cu^{2+} (954.4 eV) and Cu^{+} (952.6 eV). Similarly, the Cu $2p_{3/2}$ peak was deconvoluted into Cu^{2+} (934.5 eV) and Cu^{+} (932.8 eV) peaks. The high-resolution Mn 2p spectrum (Fig. S3(d) in the ESM) shows peaks at 641.6 and 644.0 eV corresponding to Mn^{2+} and Mn^{4+}, respectively. The characteristic peaks at 779.7 and 794.8 eV in the high-resolution Co 2p spectrum correspond to the Co $2p_{3/2}$ and Co $2p_{1/2}$ orbitals, respectively (Fig. S3(e) in the ESM). Gaussian fitting generated two Co^{3+} components at 796.0 and 780.9 eV and two Co^{2+} components at 794.6 and 779.6 eV.

Based on the mass percentage of the Ni, Zn, Cu, Mn, and Co elements obtained from ICP-OES/MS, the molar ratio of the elements of (NiZnCuMn)Co_2O_4-6 h, (NiZnCuMn)Co_2O_4-12 h, (NiZnCuMn)Co_2O_4-18 h, (NiZnCuMn)Co_2O_4-24 h, and (NiZnCuMn)Co_2O_4-30 h can be calculated to be approximately, as shown in Table S1 in the ESM. And the entropy values of each sample are 1.04R, 1.09R, 1.11R, 1.09R, and 1.11R, respectively. The value of each sample falls into the "medium-entropy" regime (1R < Sconfig < 1.5R).

The magnetic properties of the (NiZnCuMn)Co_2O_4 MEOs were further explored, as depicted in Figs. 2(h) and 2(i). All the MEOs exhibited a linear response to magnetic field variations, indicating paramagnetic behavior at room temperature.

The morphologies of the (NiZnCuMn)Co_2O_4 MEOs were characterized using scanning electron microscopy (SEM), as shown in Figs. 3(a)–3(e) and Fig. S4 in the ESM. All the samples self-assembled into fluffy spherical shapes, and their surfaces contained Ni, Zn, Cu, Mn, Co, and O elements (Fig. 3(f) and Fig. S4 in the ESM). The internal microstructure of (NiZnCuMn)Co_2O_4-18 h was further investigated by transmission electron microscopy (TEM) (Figs. 3(g)–3(k)). As shown in Figs. 3(g) and 3(h), (NiZnCuMn)Co_2O_4-18 h exhibited a spherical structure, consistent with the SEM images (Fig. 3(b)). Clear lattice fringes with lattice spacings of 0.22 and 0.25 nm, corresponding to the (222) and (311) crystal faces of cobaltate, respectively, were observed in the electron diffraction image (Fig. 3(i)). The presence of typical rings in Fig. 3(j), in accord with the crystal planes of cobaltate, indicated the polycrystalline nature of (NiZnCuMn)Co_2O_4-18 h. The element distribution of (NiZnCuMn)Co_2O_4-18 h was characterized via TEM combined with energy-dispersive spectroscopy, revealing that Ni, Zn, Cu, Mn, Co, and O were uniformly distributed at the micrometer scale (Fig. 3(k)). These results indicate that single-phase (NiZnCuMn)Co_2O_4 MEOs with a porous spherical morphology were successfully prepared at a synthesis temperature of only 400 °C.

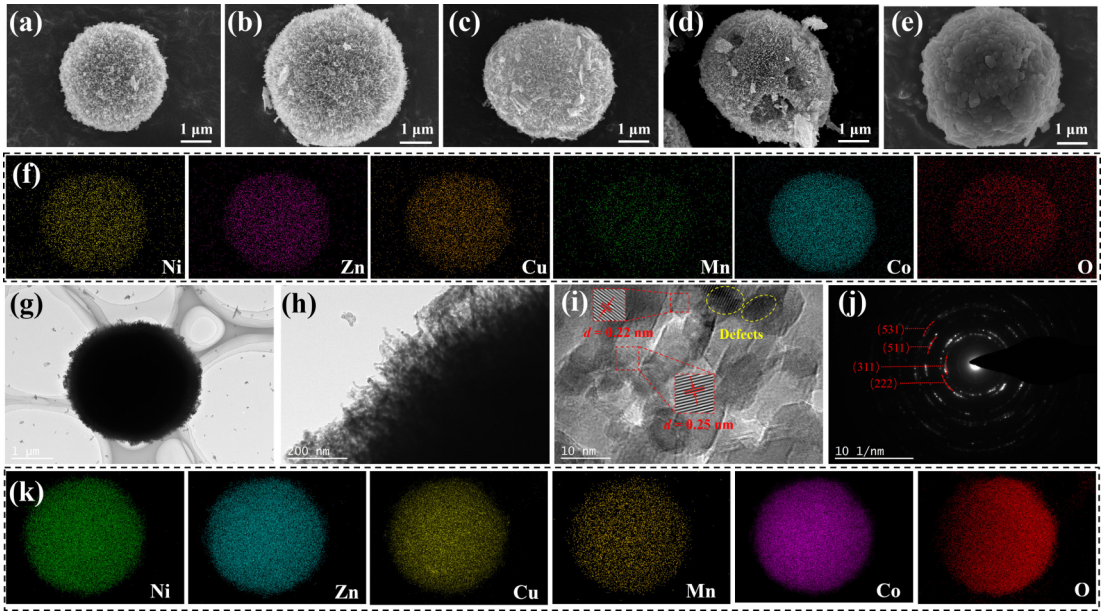

Figure 3 SEM images of (a) (NiZnCuMn)Co_2O_4-6 h, (b) (NiZnCuMn)Co_2O_4-12 h, (c) (NiZnCuMn)Co_2O_4-18 h, (d) (NiZnCuMn)Co_2O_4-24 h, and (e) (NiZnCuMn)Co_2O_4-30 h. (f) EDS mappings of (NiZnCuMn)Co_2O_4-18 h. (g) and (h) TEM images, (i) HRTEM image, (j) SAED pattern, and (k) EDS mappings of (NiZnCuMn)Co_2O_4-18 h.

To further understand the microwave absorption mechanism of the (NiZnCuMn)Co_2O_4 MEOs, their electromagnetic parameters were determined. The real part of the permittivity (ε') of (NiZnCuMn)Co_2O_4-6 h, (NiZnCuMn)Co_2O_4-12 h, (NiZnCuMn)Co_2O_4-18 h, (NiZnCuMn)Co_2O_4-24 h, and (NiZnCuMn)Co_2O_4-30 h fluctuated in the ranges of 3.17–3.78, 4.53–7.06, 4.35–7.58, 5.24–9.42, and 6.69–11.57, respectively (Fig. 4(a)). As the frequency increased, the ε' values of all MEOs decreased, indicating dispersive behavior. This phenomenon is closely related to the polarization mechanism. When EMWs penetrate (NiZnCuMn)Co_2O_4, the spinel structure produces a polarization response to the electromagnetic field. As the frequency increases, the intrinsic electric dipole moment of the material gradually lags behind the change in external field, resulting in energy dissipation and the corresponding decrease in the real part of the dielectric constant [31]. (NiZnCuMn)Co_2O_4-6 h, (NiZnCuMn)Co_2O_4-12 h, (NiZnCuMn)Co_2O_4-18 h, (NiZnCuMn)Co_2O_4-24 h, and (NiZnCuMn)Co_2O_4-30 h exhibited average ε' values of 3.34, 5.27, 5.34, 6.49, and 7.76, respectively, and average ε'' values of 0.58, 1.40, 2.53, 1.73, and 2.85, respectively (Fig. 4(b)). In addition, several resonance peaks were observed in the 8–14 GHz range, which are indicative of a significant relaxation process [32]. The dielectric loss tangents ($\tan\delta_\varepsilon$, Fig. 4(c)) exhibited a similar trend to that of ε''. Accordingly, the dielectric loss capacities of (NiZnCuMn)Co_2O_4-6 h, (NiZnCuMn)Co_2O_4-12 h, (NiZnCuMn)Co_2O_4-18 h, (NiZnCuMn)Co_2O_4-24 h, and (NiZnCuMn)Co_2O_4-30 were determined to be 0.17, 0.26, 0.48, 0.26, and 0.36, respectively. Thus, (NiZnCuMn)Co_2O_4-18 h exhibited a strong dielectric loss capacity.

(NiZnCuMn)Co_2O_4-6 h, (NiZnCuMn)Co_2O_4-12 h, (NiZnCuMn)Co_2O_4-18 h, (NiZnCuMn)Co_2O_4-24 h, and (NiZnCuMn)Co_2O_4-30 h also exhibited fluctuating values for the real part of permeability (μ') of 0.93–1.11, 0.88–1.01, 0.95–1.10, 0.76–0.92, and 0.81–0.88, respectively (Fig. 4(d)), and fluctuating values for the imaginary part of permeability (μ'') ranging from 1.2×10^{-5} to 0.12, 2.8×10^{-4} to 0.07, 5.6×10^{-3} to 0.15, 0.05 to 0.21, and 0.01 to 0.10, respectively (Fig. 4(e)). The fluctuations of the real and imaginary parts of the permeability over the frequency range of 8–14 GHz indicate magnetic resonance losses, which can be attributed to exchange resonance [33]. The magnetic loss tangent ($\tan\delta_\mu$) represents the dielectric–magnetic loss capabilities [30]. The average $\tan\delta_\mu$ decreased in the order (NiZnCuMn)Co_2O_4-24 h > (NiZnCuMn)Co_2O_4-18 h > (NiZnCuMn)Co_2O_4-30 h > (NiZnCuMn)Co_2O_4-12 h > (NiZnCuMn)Co_2O_4-6 h (Fig. 4(f)). Furthermore, comparing Figs. 4(c) and 4(f) reveals that $\tan\delta_\varepsilon > \tan\delta_\mu$, indicating that the absorption capacity of the (NiZnCuMn)Co_2O_4 MEOs mainly depends on the dielectric loss [34].

To analyze the dielectric loss mechanism, the Cole–Cole curves of (NiZnCuMn)Co_2O_4-6 h, (NiZnCuMn)Co_2O_4-12 h, (NiZnCuMn)Co_2O_4-18 h, (NiZnCuMn)Co_2O_4-24 h, and (NiZnCuMn)Co_2O_4-30 h are depicted in Figs. 4(g)–4(k) and Fig. S5(a) in the ESM. Debye relaxation is an important indicator of the interface polarization phenomenon and can be expressed by the Debye formula as follows

$$\left(\varepsilon' - \frac{\varepsilon_s + \varepsilon_\infty}{2}\right)^2 + (\varepsilon'')^2 = \left(\frac{\varepsilon_s - \varepsilon_\infty}{2}\right)^2 \quad (6)$$

where ε_s and ε_∞ are the static and optical dielectric constant, respectively. ε' and ε'' represent the real part and the imaginary part of the dielectric constant [35, 36]. Polarization relaxation and conduction loss contributed to the dielectric loss in all MEOs. The appearance of Cole–Cole semicircles indicates the existence of a Debye relaxation process [37]. The Cole–Cole curves exhibited 3–7 semicircular curves at the high-frequency band, indicating multiple dipole polarization-induced Debye relaxation mechanisms under an electromagnetic field. In particular, the presence of many irregular and distorted semicircles indicated the occurrence of other mechanisms, such as defect polarization [38]. The conduction loss can be inferred from the linear characteristics of the tails of the curves; the greater the slope of this linear segment, the greater the conductivity loss in the material.

Magnetic loss is mainly attributed to eddy current loss, natural resonance at gigahertz frequencies, and exchange resonance. If the C_0 value remains constant within a certain frequency range, then eddy current loss is considered to be the main contributing factor to

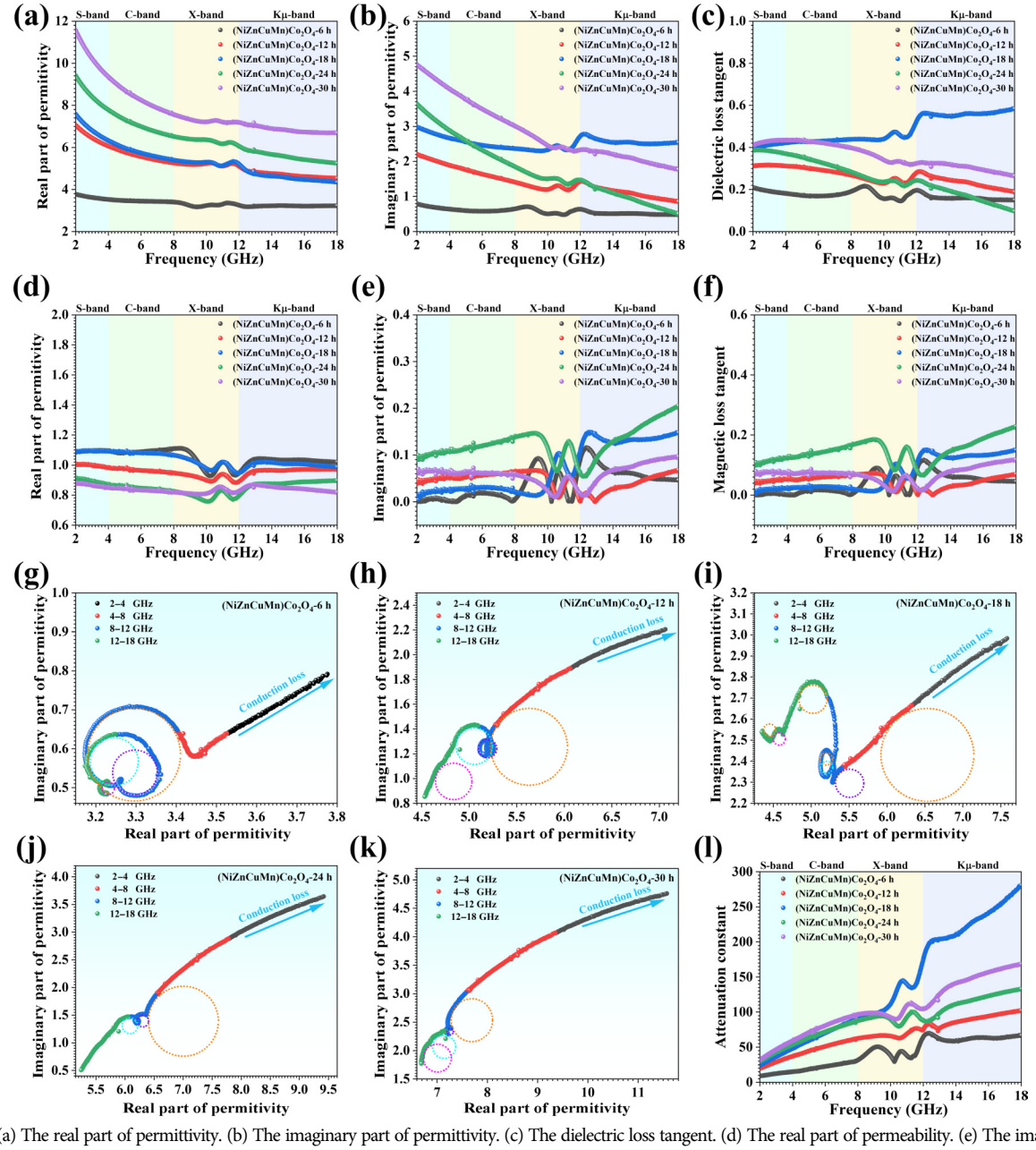

Figure 4 (a) The real part of permittivity. (b) The imaginary part of permittivity. (c) The dielectric loss tangent. (d) The real part of permeability. (e) The imaginary part of permeability. (f) The magnetic loss tangent. The single Cole–Cole curves of (g) (NiZnCuMn)Co_2O_4-6 h, (h) (NiZnCuMn)Co_2O_4-12 h, (i) (NiZnCuMn)Co_2O_4-18 h, (j) (NiZnCuMn)Co_2O_4-24 h, and (k) (NiZnCuMn)Co_2O_4-30 h. (l) The attenuation constant of (NiZnCuMn)Co_2O_4 with different hydrothermal time.

magnetic loss [39]. As shown in Fig. S5(b) in the ESM, within the range of 2–18 GHz, all the C_0 curves showed significant fluctuations, which indicated that both natural resonance and exchange resonance also play a role in magnetic loss. As shown in Fig. 4(i), the slope of this linear segment at the low-frequency band was the largest for (NiZnCuMn)Co_2O_4-18 h, which is indicative of its greatest conductivity loss among the MEOs.

The attenuation constant is an index of the capacity to dissipate the EMW energy. Figure 4(l) shows the attenuation constants of (NiZnCuMn)Co_2O_4-6 h, (NiZnCuMn)Co_2O_4-12 h, (NiZnCuMn)Co_2O_4-18 h, (NiZnCuMn)Co_2O_4-24 h, and (NiZnCuMn)Co_2O_4-30 h. The average attenuation capacities decreased in the order α(NiZnCuMn)Co_2O_4-18 h (137.74) > α(NiZnCuMn)Co_2O_4-30 h (105.22) > α(NiZnCuMn)Co_2O_4-24 h (88.90) > α(NiZnCuMn)Co_2O_4-12 h (66.80) > α(NiZnCuMn)Co_2O_4-6 h (41.47), revealing that (NiZnCuMn)Co_2O_4-18 h exhibited the strongest attenuation capacity. In addition, the attenuation capacity of (NiZnCuMn)Co_2O_4-30 h was higher than that of the others in the low-frequency range.

As shown in Figs. 5(a), 5(d), 5(g), 5(j), and 5(m), and Figs. S6(a)–S6(f) in the ESM, the RL_{min} and EAB of (NiZnCuMn)Co_2O_4-6 h, (NiZnCuMn)Co_2O_4-12 h, (NiZnCuMn)Co_2O_4-18 h, (NiZnCuMn)Co_2O_4-24 h, and (NiZnCuMn)Co_2O_4-30 h were −8.58 dB (3.78 mm) and 0 GHz, −14.15 dB (4.79 mm) and 2.04 GHz (4.22 mm), −64.05 dB (2.95 mm) and 7.35 GHz (2.66 mm), −65.78 dB (4.36 mm) and 3.58 GHz (2.65 mm), and −58.66 dB (3.38 mm) and 5.01 GHz (2.11 mm), respectively. The two-dimensional (2D) RL mapping diagrams of (NiZnCuMn)

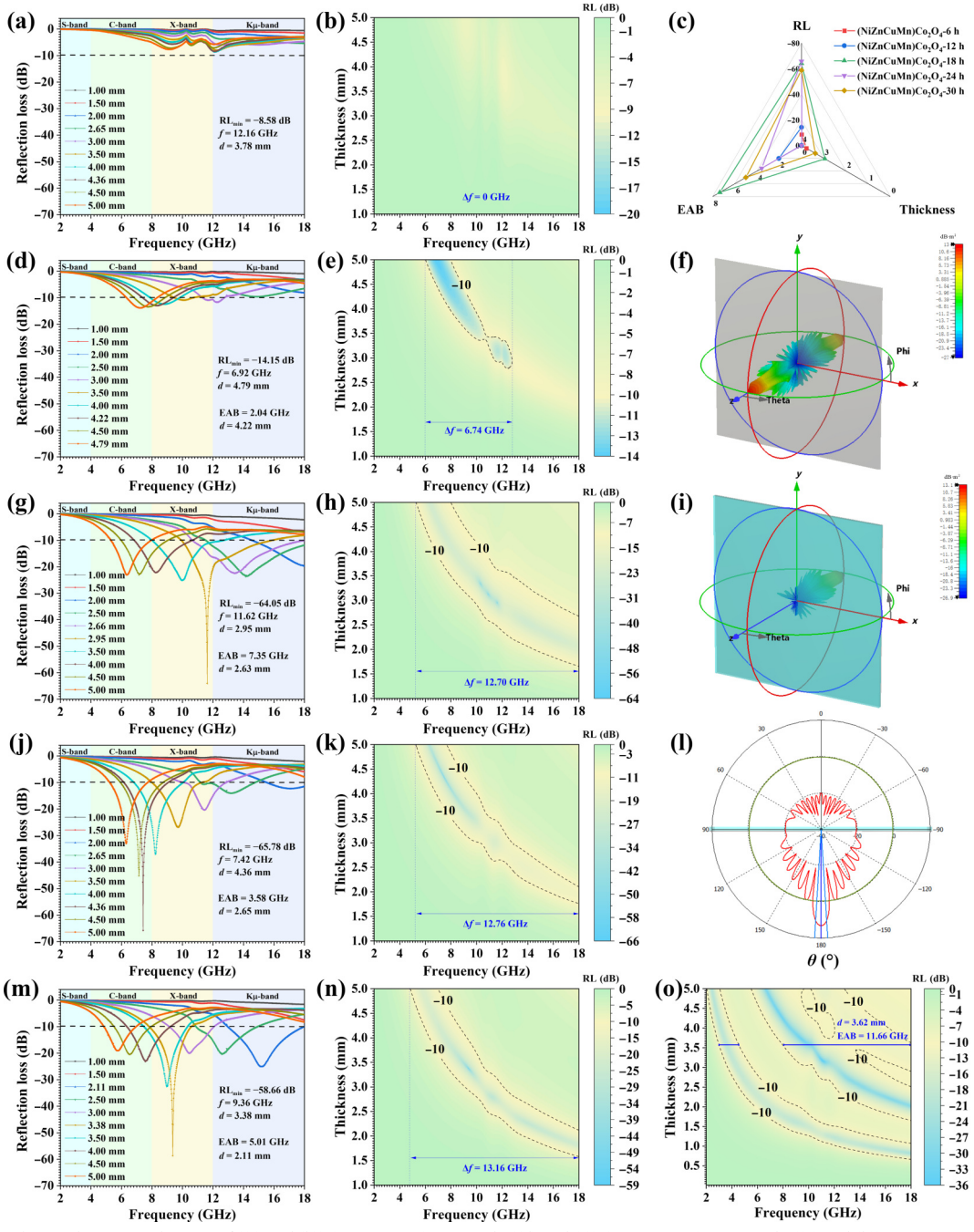

Figure 5 2D RL values and mapping diagram of ((a) and (b)) (NiZnCuMn)Co_2O_4-6 h, ((d) and (e)) (NiZnCuMn)Co_2O_4-12 h, ((g) and (h)) (NiZnCuMn)Co_2O_4-18 h, ((j) and (k)) (NiZnCuMn)Co_2O_4-24 h, and ((m) and (n)) (NiZnCuMn)Co_2O_4-30 h. (c) Performance comparison of all samples. 3D radar wave scattering signals of (f) PEC and (i) (NiZnCuMn)Co_2O_4-18 h. (l) The RCS values of the (NiZnCuMn)Co_2O_4-18 h on PEC under different scanning angles. (o) 2D RL contour map of the (NiZnCuMn)Co_2O_4-6 h + (NiZnCuMn)Co_2O_4-18 h + (NiZnCuMn)Co_2O_4-24 h with three-layer structure.

Co_2O_4-6 h, (NiZnCuMn)Co_2O_4-12 h, (NiZnCuMn)Co_2O_4-18 h, (NiZnCuMn)Co_2O_4-24 h, and (NiZnCuMn)Co_2O_4-30 h are shown in Figs. 5(b), 5(e), 5(h), 5(k), and 5(n). Adjusting the sample thickness resulted in effective EMW absorption values (RL ≤ −10 dB) of 0, 6.74, 12.70, 12.76, and 13.16 GHz in the frequency range of 2–18 GHz, indicating that the coverage ranges were 0%, 42.13%, 79.38%, 79.75%, and 82.25%, respectively. As depicted in Fig. 5(c), (NiZnCuMn)Co_2O_4-18 h possessed a thin matching thickness, strong RL_{min}, and broad EAB, meeting the requirements for EMW absorbing materials.

To study the actual radar stealth effect of the (NiZnCuMn)Co_2O_4 MEOs, the RCS of the fabricated absorbing material was simulated using computer simulation technology (CST) with the Studio Suite software. The smaller the area in the positive direction of the *Z*-axis, the better the EMW absorption performance of the material. The three-dimensional (3D) RCS reflection of a PEC is shown in Fig. 5(f). Figure 5(i) and Figs. S7(a)–S7(f) in the ESM showed the 3D RCS reflection of different samples coating a PEC plate. (NiZnCuMn) Co2O4-18 h with PEC demonstrated excellent microwave attenuation performance compared with other samples and the PEC model, underscoring its potential for practical applications. In addition, the 2D simulated RCS of the (NiZnCuMn)Co_2O_4 MEOs

from −60° to 60° are shown in Fig. S7(a) in the ESM. Compared with the PEC model, the RCS values of the five MEOs decreased. The RCS reductions of all the samples were calculated at seven detection angles (0°, 10°, 20°, 30°, 40°, 50°, and 60°) by subtracting the RCS of the PEC base (Fig. S7(b) in the ESM). As shown in Fig. 5(l) and Figs. S8(a)–S8(e) in the ESM, the one-dimensional RCS reflection of (NiZnCuMn)Co_2O_4-18 h demonstrated its excellent microwave attenuation performance.

The effective impedance matching (Z_m = Z_{in}/Z_0) of a high-performance microwave absorber (RL < −10 dB) ranges from 0.53 to 1.93 [39], which ensures that EMWs penetrate the material. The 2D mapping of Z_m for (NiZnCuMn)Co_2O_4-6 h, (NiZnCuMn)Co_2O_4-12 h, (NiZnCuMn)Co_2O_4-18 h, (NiZnCuMn)Co_2O_4-24 h, and (NiZnCuMn)Co_2O_4-30 h is shown in Figs. S9(a)–S9(e) in the ESM, respectively. The area proportions of the Z_m values between 0.53 and 1.93 for each MEO were 40.90%, 44.81%, 45.90%, 40.98%, and 35.16%, respectively. The superior impedance matching effect area of (NiZnCuMn)Co_2O_4-18 h (0.53–1.93) compared with that of the other MEOs indicates that more EMWs can penetrate the material (Fig. S9(c) in the ESM). Moreover, the relationship between RL and Z_m shows the rational material design (Fig. S10 in the ESM). When the RL values reach their minimum, the corresponding values of Z_m are approximately 1 for (NiZnCuMn)Co_2O_4-18 h, (NiZnCuMn)Co_2O_4-24 h, and (NiZnCuMn)Co_2O_4-30 h. The electromagnetic wave absorption performance of (NiZnCuMn)Co_2O_4-6 h and (NiZnCuMn)Co_2O_4-12 h was poor due to suboptimal impedance matching.

As shown in Fig. 5(o), when each layer had a thickness of 3.62 mm, the three layers material achieved 11.66 GHz (3.62 mm). It covered 2.96–4.46 and 7.88–18 GHz achieving the whole X-band and Kμ-band absorption.

The (NiZnCuMn)Co_2O_4 MEOs outperformed most advanced medium-entropy EMW absorbers in terms of EMW absorption (Table 1) [17, 29, 40–48]. For (NiZnCuMn)Co_2O_4-18 h, the RL_{min} value was −64.05 dB at a matching thickness of 2.95 mm and the EAB value was 7.35 GHz at a matching thickness of 2.66 mm. In addition, compared with reported materials, the (NiZnCuMn)Co_2O_4 MEOs were sintered at a much lower temperature (400 °C) (Table 1).

Figure 6 illustrates the microwave absorption mechanism of (NiZnCuMn)Co_2O_4. The incident microwaves are repeatedly reflected and scattered among Ni, Zn, Cu, Mn, Co, and O atoms, consuming part of the energy. These multiple reflections and scattering of EMWs are promoted by the stacking of spherical (NiZnCuMn)Co_2O_4 particles, which form a complex 3D structure. The spherical structures of Ni, Zn, Cu, Mn, Co, and O atoms also create a 3D network that provides good paths for electron hopping and transitions, thereby increasing the conductive loss. During the

Table 1 The comparison of this work and the other reported advanced EMW absorbers

	Materials	Preparation temperature (°C)	RL_{min} (dB)	EAB (GHz)	Refs.
1	$(FeCo_{0.2}Ni_{0.2}Cr_{0.2}Mn_{0.2})O_4$	1000	−41.6	6.1	[41]
2	$(Ba_{1/3}Sr_{1/3}Ca_{1/3})FeO_3$	1100	−40.58	4.16	[40]
3	$(FeCoNiZn)_xV_2O_y$	900	−36.50	2.77	[42]
4	(MgCoNiCuZn)O	1100	−41.35	2.92	[43]
5	$(Ca_{0.2}Sr_{0.2}Ba_{0.2}La_{0.2}Pb_{0.2})TiO_3$	1150	−17.6	1.4	[44]
6	$(V_{0.2}Nb_{0.2}Zr_{0.2}Ta_{0.2}Ti_{0.2})B_2$	1900	−40.70	2.30	[45]
7	$(Hf,Ta,V,W,Ti,Mo,Nb,Zr,Co)B_2$	2000	−42.60	7.20	[29]
8	$(Ce_{0.2}Y_{0.2}Sm_{0.2}Er_{0.2}Yb_{0.2})B_6$	1900	−33.40	3.90	[46]
9	$(Ti_{0.2}Zr_{0.2}Mo_{0.2}Nb_{0.2}Ta_{0.2})C$	1800	−36.6	5.00	[17]
10	$(Ti_{0.2}Zr_{0.2}Hf_{0.2}Nb_{0.2}Ta_{0.2})C$	1900	−38.50	2.30	[47]
11	$(HfTaZrTiNbMoWCr)C_8$	1800	−43.63	5.12	[48]
12	(NiZnCuMn)Co_2O_4	400	−64.05	7.35	This work

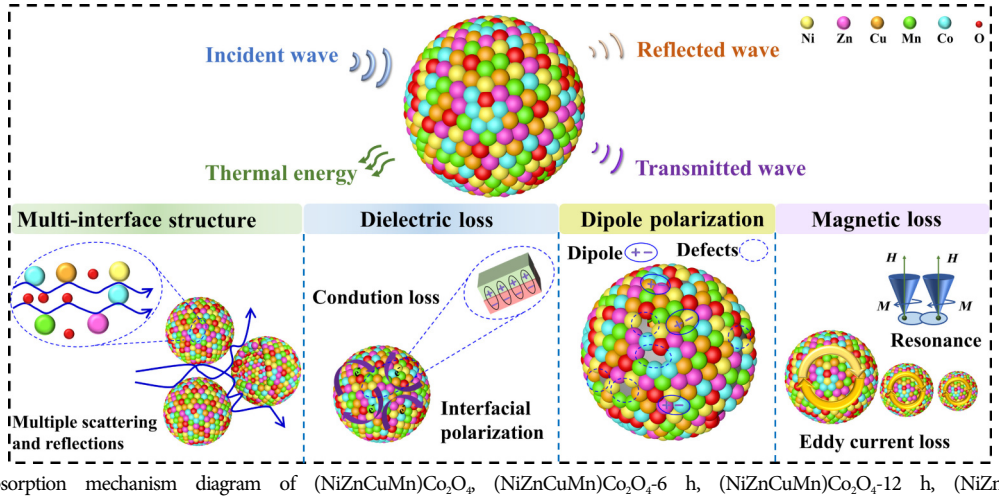

Figure 6 EMW absorption mechanism diagram of (NiZnCuMn)Co_2O_4, (NiZnCuMn)Co_2O_4-6 h, (NiZnCuMn)Co_2O_4-12 h, (NiZnCuMn)Co_2O_4-18 h, (NiZnCuMn)Co_2O_4-24 h, and (NiZnCuMn)Co_2O_4-30 h.

high-temperature sintering process in a muffle furnace, abundant point defects and lattice distortions are generated inside the MEO, resulting in a large number of dipole moments. Finally, because of the eddy current and resonance effects of the MEO, the magnetic loss performance is further improved. Under the combined effect of multiple losses, the MEO achieves microwave absorption over a wide frequency range.

Electrochemical tests were performed in a 3.5 wt.% NaCl solution. The open-circuit potential (OCP) was measured for 600 s before stabilizing (Fig. S11 in the ESM). As the soaking time increased, the OCP values decreased to varying degrees. (NiZnCuMn)Co_2O_4-18 h showed the highest OCP values among the samples, indicating that it effectively inhibited corrosion.

To conduct an in-depth analysis of the coating, an equivalent circuit (EC) was introduced to describe and fit the AC impedance using the ZView software, as shown in Fig. 7(a). In the circuits, R_s, CPE_c, R_c, CPE_{dl}, and R_{ct} represent the solution resistance, the passive film capacitance, the passive film resistance, the double-layer capacitance, and the charge transfer resistance, respectively. The EIS data were fitted using EC, and the resulting curves are shown in Fig. 7(a).

Figure 7(b) shows the Nyquist plots of the (NiZnCuMn)Co_2O_4 at 0-day corrosion. The coating initially exhibited a relatively low impedance value. As the hydrothermal time increased, the impedance value gradually increased. The film doped with (NiZnCuMn)Co_2O_4-18 h showed larger radii, indicating higher initial impedance values, followed by a decrease after 24 h. This phenomenon indicated the presence of a passivation layer and a spatial potential barrier effect in the coating.

Figures 7(c), 7(f), 7(i), 7(l), and 7(o) show the Nyquist plots of the EIS of the (NiZnCuMn)Co_2O_4 at OCP. All MEOs showed a small semicircular arc and a larger semicircular arc. The radius of the Nyquist plots correlated with the corrosion resistance. As the soaking time increased, the radii of the Nyquist plots decreased, indicating the gradual penetration of the corrosive medium.

The Bode plots are shown in Figs. 7(d), 7(g), 7(j), 7(m), and 7(p). Generally, the low-frequency impedance modulus ($|Z|_{0.01\ Hz}$) serves as a semiquantitative indicator of the ability of a coating to resist corrosive media [32]. As the soaking time in 3.5 wt.% NaCl increased, $|Z|_{0.01\ Hz}$ decreased. At 0-day of immersion, (NiZnCuMn)Co_2O_4-18 h showed the highest $|Z|_{0.01\ Hz}$ value of 1.6×10^5 Ω·cm^2. After 14 days of immersion, the $|Z|_{0.01\ Hz}$ value of (NiZnCuMn)Co_2O_4-18 h decreased from 10^5 to 10^3 Ω·cm^2. Thus, the corrosion resistance of the coating decreased with increasing soaking time.

According to the phase angle principle, values close to 0 indicate highly capacitive electrochemical reactions, whereas a phase angle close to 90° indicates higher resistance and a slower reaction rate [14]. As shown in Figs. 7(e), 7(h), 7(k), 7(n), and 7(q), the phase angle plots showed a linear relationship at high frequencies but gradually shifted downward at low frequencies. As the soaking time increased, the phase angle gradually decreased, reflecting an increase in the coating surface roughness [49]. At 0-day corrosion, the phase angle plots of (NiZnCuMn)Co_2O_4-18 h were the highest, indicating its superior corrosion resistance.

The Tafel polarization curves of the (NiZnCuMn)Co_2O_4 MEOs after corrosion for different durations are shown in Figs. 8(a)–8(e), and the corresponding corrosion parameters are shown in Table 2. Generally, a lower corrosion current density (I_{corr}) and a higher corrosion potential (E_{corr}) indicate a slower corrosion rate and superior corrosion resistance [32, 50]. As shown in Fig. 8(f), among the MEOs, (NiZnCuMn)Co_2O_4-6 h displayed the lowest I_{corr} (7.58×10^{-8} A/cm^2), and (NiZnCuMn)Co_2O_4-24 h exhibited the highest E_{corr} of −0.424 V. These results indicate that the hydrothermal reaction time could be tuned to meet specific requirements. As shown in Fig. 8(g), after immersion in 3.5 wt.% NaCl solution for 14 days, I_{corr} decreased in the order (NiZnCuMn)Co_2O_4-12 h < (NiZnCuMn)Co_2O_4-18 h < (NiZnCuMn)Co_2O_4-6 h < (NiZnCuMn)Co_2O_4-30 h < (NiZnCuMn)Co_2O_4-24 h. (NiZnCuMn)Co_2O_4-12 h displayed the lowest corrosion current (6.61×10^{-6} A/cm^2), closely followed by (NiZnCuMn)Co_2O_4-18 h (6.66×10^{-6} A/cm^2). Meanwhile, (NiZnCuMn)Co_2O_4-18 h exhibited the highest E_{corr} of −0.712 V. Overall, (NiZnCuMn)Co_2O_4-18 h demonstrated better corrosion resistance.

As shown in Fig. 8(h), the formation of abundant cracks and pores during the curing process of the pure epoxy resin (EP) coating provided more channels for corrosive substances such as H_2O, O_2, and Cl^- to penetrate the coating, leading to corrosion of the metal substrate. After their addition, the (NiZnCuMn)Co_2O_4 MEOs filled the defects (e.g., gaps and pores) in EP, making the path for corrosive media to reach the metal substrate more tortuous, thereby improving the corrosion resistance of the coating (Fig. 8(i)). Compared with similar absorbing and anticorrosion materials, the (NiZnCuMn)Co_2O_4 MEOs can be prepared at a lower temperature and exhibit a wider EAB and excellent corrosion resistance (Table S2 in the ESM). The SEM morphology of the composite EP coating was shown in Figs. S12(a)–S12(e) in the ESM, the coating was relatively smooth. After the TAFEL test, some corrosion products were dispersed in the coating (Figs. S12(f)–S12(j) in the ESM). After being immersed in 3.5 wt.% NaCl for 14 days and undergoing electrochemical testing, the surface morphology of the coating was tested, as shown in Figs. S12(k)–S12(o) in the ESM. In Figs. S12(k) and S12(l) in the ESM, it can be clearly observed that there are numerous bubbles in the layers. This might be due to the accumulation of corrosion products beneath the coating, which led to a decrease in the adhesion between the coating and the substrate, thereby causing the bubbling.

4 Conclusions

(NiZnCuMn)Co_2O_4 MEOs with microwave absorption and anticorrosion properties were successfully fabricated using a hydrothermal reaction. Owing to its unique structure, (NiZnCuMn)Co_2O_4-18 h showed an RL_{min} of −64.05 dB (2.95 mm) and an ultrabroad EAB of 7.35 GHz (2.66 mm). CST simulation demonstrated the application potential of (NiZnCuMn)Co_2O_4 in radar stealth applications. Furthermore, adjusting the duration of the hydrothermal reaction enabled the preparation of (NiZnCuMn)Co_2O_4 coatings with excellent anticorrosion properties. This work provides new insights into the fabrication of highly entropic magnetic materials for application in marine environments.

Electronic Supplementary Material: Supplementary material (results of TG and DTG test; XPS test; SEM images; Cole–Cole curves and C_0 curves; the 3D RL values with different thickness and frequency; RCS values; RCS reduction curves; 3D radar wave scattering signals; 1D radar wave scattering signals; 2D mapping of impedance matching; The RL_{min} values curve to impedance matching values; OCP test; Table S1 comparison this work with

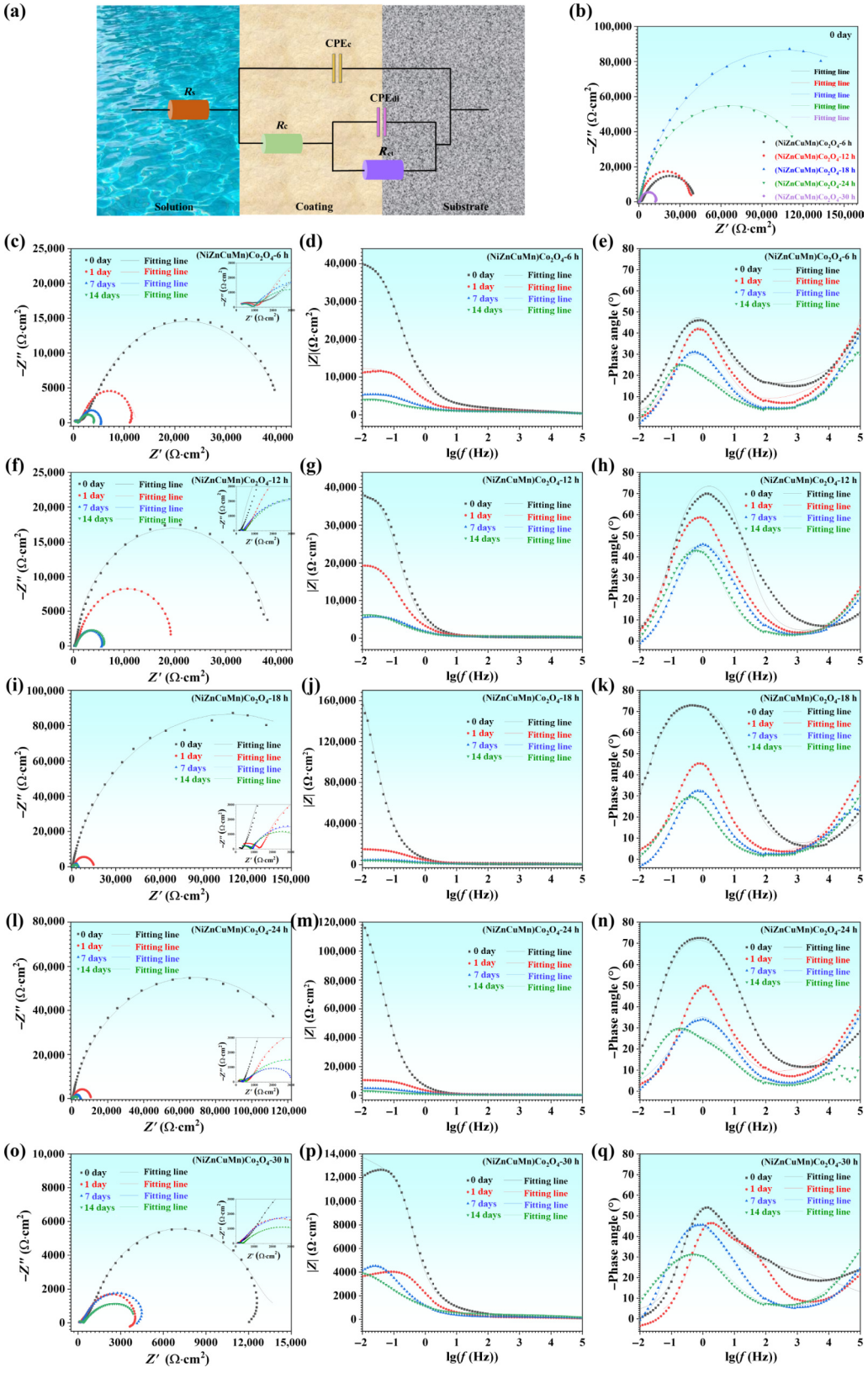

Figure 7 (a) Electrical equivalent circuit model of composite coatings. (b) Nyquist plots of (NiZnCuMn)Co_2O_4 with different hydrothermal time after 0 day corrosion. Nyquist plots of (NiZnCuMn)Co_2O_4 after 0 day, 1 day, 7 days, and 14 days corrosion: (c) (NiZnCuMn)Co_2O_4-6 h, (f) (NiZnCuMn)Co_2O_4-12 h, (i) (NiZnCuMn)Co_2O_4-18 h, (l) (NiZnCuMn)Co_2O_4-24 h, and (o) (NiZnCuMn)Co_2O_4-30 h. Porter plots of (NiZnCuMn)Co_2O_4 after 0 day, 1 day, 7 days, and 14 days corrosion: (d) (NiZnCuMn)Co_2O_4-6 h, (g) (NiZnCuMn)Co_2O_4-12 h, (j) (NiZnCuMn)Co_2O_4-18 h, (m) (NiZnCuMn)Co_2O_4-24 h, (p) (NiZnCuMn)Co_2O_4-30 h. Phase angle plots of (NiZnCuMn)Co_2O_4 after 0 day, 1 day, 7 days, and 14 days corrosion: (e) (NiZnCuMn)Co_2O_4-6 h, (h) (NiZnCuMn)Co_2O_4-12 h, (k) (NiZnCuMn)Co_2O_4-18 h, (n) (NiZnCuMn)Co_2O_4-24 h, and (q) (NiZnCuMn)Co_2O_4-30 h.

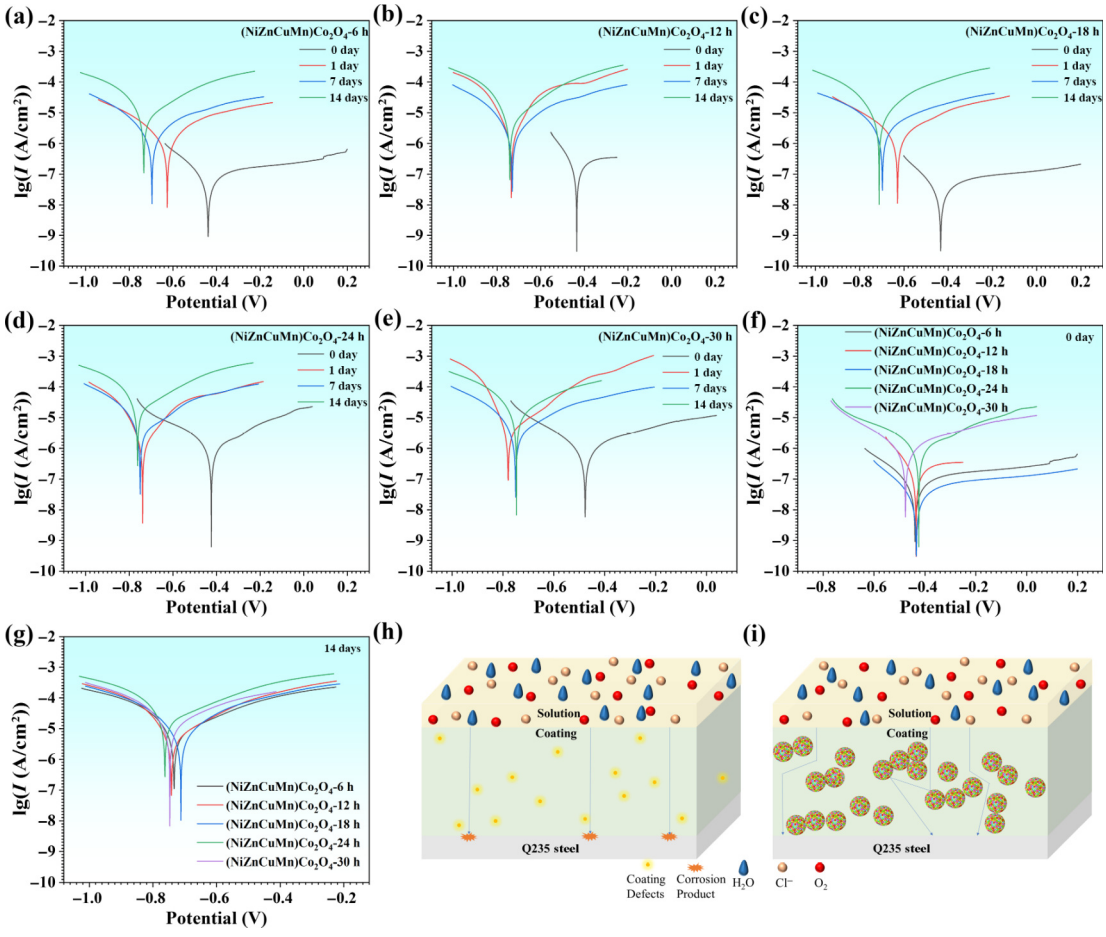

Figure 8 Tafel polarization curves with different days: (a) (NiZnCuMn)Co_2O_4-6 h, (b) (NiZnCuMn)Co_2O_4-12 h, (c) (NiZnCuMn)Co_2O_4-18 h, (d) (NiZnCuMn)Co_2O_4-24 h, and (e) (NiZnCuMn)Co_2O_4-30 h. Tafel polarization curves of (NiZnCuMn)Co_2O_4 with different hydrothermal time after (f) 0 day and (g) 14 days corrosion in 3.5 wt.% NaCl solution. Corrosion protection mechanism of the sample: (h) pure EP and (i) (NiZnCuMn)Co_2O_4/EP.

Table 2 Electrochemical corrosion parameters of different coatings

Sample	Time (day)	β_c	β_a	I_{corr} (A/cm^2)	E_{corr} (V vs. SCE)
(NiZnCuMn)Co_2O_4-6 h	0	6.875	3.151	7.581×10^{-8}	−0.438
	1	6.668	5.528	1.164×10^{-6}	−0.626
	7	7.162	5.569	1.554×10^{-6}	−0.696
	14	6.830	4.780	9.528×10^{-6}	−0.733
(NiZnCuMn)Co_2O_4-12 h	0	9.487	2.015	2.358×10^{-7}	−0.435
	1	10.948	10.496	1.896×10^{-6}	−0.735
	7	7.821	6.343	2.139×10^{-6}	−0.731
	14	8.224	5.633	6.608×10^{-6}	−0.742
(NiZnCuMn)Co_2O_4-18 h	0	7.616	2.263	2.382×10^{-7}	−0.466
	1	5.747	4.534	1.964×10^{-6}	−0.629
	7	6.191	4.540	2.940×10^{-6}	−0.697
	14	7.798	6.462	6.656×10^{-6}	−0.712
(NiZnCuMn)Co_2O_4-24 h	0	5.107	3.124	1.612×10^{-6}	−0.424
	1	9.834	8.965	1.698×10^{-6}	−0.739
	7	6.938	4.410	5.575×10^{-6}	−0.750
	14	6.312	4.384	3.237×10^{-5}	−0.762
(NiZnCuMn)Co_2O_4-30 h	0	6.018	4.082	9.978×10^{-7}	−0.477
	1	13.191	5.454	4.423×10^{-6}	−0.779
	7	7.148	5.068	4.105×10^{-6}	−0.750
	14	6.811	4.985	1.631×10^{-5}	−0.747

reported materials) is available in the online version of this article at https://doi.org/10.26599/NR.2026.94908562.

Data availability

All data needed to support the conclusions in the paper are presented in the manuscript and the Electronic Supplementary Material. Additional data related to this paper may be requested from the corresponding author upon request.

Acknowledgements

This work was supported by Science Foundation of Jiangxi Provincial Department of Education (No. GJJ2400915), the Early Career Youth Science and Technology Talent Training Project of Jiangxi Province (No. 20244BCE52206), the Opening Project of Material Corrosion and Protection Key Laboratory of Sichuan province (No. 2025CL09), the National Natural Science Foundation of China (No. 52362003), Science and Technology Planning Project of Jingdezhen (No. 2023GY001-14), and Key Project of Jiangxi Association for Science Education (No. 2025KXJYS046).

Declaration of competing interest

All the contributing authors report no conflict of interests in this work.

Author contribution statement

D. D. M.: Validation, writing manuscript. S. H. C.: Data curation. J. J. Q.: Writing – review & editing, supervision, funding acquisition. Y. Q. W.: Funding acquisition, conceptualization, supervision. M. M. B.: Investigation, formal analysis. H. H. G.: Formal analysis. C. Y.: Data curation. X. Z. Z.: Conceptualization.

Use of AI statement

None.

References

[1] Qian, J. J.; Ma, D. D.; Zou, Y. X.; Zheng, L. L.; Liang, Y.; Wang, S. H.; Zhou, X. L.; Cheng, X. Y.; Shan, Q. L.; Wang, Y. Q. Implanting Ag nanoparticles in SiOC ceramic nanospheres for exceptional electromagnetic wave absorption and antibacterial performance. *J. Adv. Ceram.* **2025**, *14*, 9221084.

[2] Xu, J. J.; Wang, L.; Wang, X. M.; Qiu, H. P. Research progress of high temperature absorbing materials. *Adv. Ceram.* **2024**, *45*, 189–205.

[3] Wu, X.; Kang, P. Y.; Zhang, Y. H.; Guo, H. C.; Yang, S. Y.; Zheng, Q.; Wang, L. J.; Jiang, W. Highly electrically conductive MOF/conducting polymer nanocomposites toward tunable electromagnetic wave absorption. *J. Mater. Sci. Technol.* **2025**, *205*, 258–269.

[4] Tang, P.; Zhao, X. Y.; Du, J. W.; Li, M.; Qian, H. N.; Ren, H. Q.; Zhang, X. Y.; Wu, G. H.; Wang, X. W. Hollow core–shell Co@SiO_2@PPy composites with efficient electromagnetic wave absorption. *Appl. Surf. Sci.* **2024**, *660*, 159977.

[5] Kumari, S.; Dalal, J.; Kumar, A.; Pal, R.; Chahal, R.; Ohlan, A. Enhanced microwave absorption properties of conducting polymer@graphene composite to counteract electromagnetic radiation pollution: Green EMI shielding. *RSC Adv.* **2024**, *14*, 662–676.

[6] Liu, C. Y.; Cai, Y. F.; Liang, T. C.; Zang, T. Z.; Fei, G. X.; Xia, H. S. Additive manufacturing flexible, conductive and self-healing polydimethylsiloxane carbon nanotubes composites for electromagnetic interference shielding and microwave absorption. *Chem. Eng. J.* **2025**, *520*, 165717.

[7] Qian, J. J.; Ma, D. D.; Zhou, X. L.; Liao, H. M.; Shan, Q. L.; Wang, S. H.; Wang, Y. Q.; Zeng, X. J. Synthesis of SiOC@C ceramic nanospheres with tunable electromagnetic wave absorption performance. *J. Adv. Ceram.* **2024**, *13*, 1394–1408.

[8] Fan, X.; Li, B. Y.; Zi, W. H.; Kang, M. L.; Wu, H. D.; Bian, J. P.; Sun, M. Y. Microwave dielectric characterization and loss mechanism of biowaste during pyrolysis. *Energy Convers. Manage.* **2024**, *301*, 118075.

[9] Wang, F. Y.; Liu, Y. L.; Feng, R. D.; Wang, X.; Han, X. J.; Du, Y. C. A "win-win" strategy to modify Co/C foam with carbon microspheres for enhanced dielectric loss and microwave absorption characteristics. *Small* **2023**, *19*, 2303597.

[10] Khanahmadi, S.; Masoudpanah, S. M. Preparation and microwave absorption properties of $CoFe_2O_4$/$NiCo_2O_4$ composite powders. *Ceram. Int.* **2024**, *50*, 9779–9788.

[11] Xu, S.; Liu, Q. H.; Yu, Z. L.; Dai, X. D.; Yu, S. Y.; Li, C. J. Reduction-regulated ultralight $CoFe_2O_4$ nanofiber/graphene composite aerogels as superior broadband electromagnetic wave absorber. *Carbon* **2025**, *234*, 119859.

[12] Zhu, S. S.; Guo, X. J.; Xiang, R.; Cheng, L. C.; Ye, F. X.; Li, Z. C.; Yao, Q. R.; Qi, H. Y.; Long, Q. X. Balance dielectric and magnetic losses to enhance the microwave absorption performance of $CaFe_{0.5}Mn_{0.5}O_{3-\delta}$@$Co_3O_4$@$Fe_3O_4$. *J. Alloys Compd.* **2025**, *1020*, 179194.

[13] Wei, S.; Sun, T. X.; Ma, C. C.; Gao, H.; Zhao, Z. P.; Feng, H. M.; Li, W.; Chen, S. G. Improved interfacial interactions by core–shell $CoFe_2O_4$@SiO_2 composites to enhance the ability of corrosion resistance and electromagnetic wave absorption. *Small* **2024**, *20*, 2405814.

[14] Zhang, F.; Wu, L. J.; Su, H. M.; Jiang, J. H.; Tian, J. H.; Sun, K.; Cheng, C. B.; Lei, Y. H.; Fan, R. H. Electromagnetic wave absorption and corrosion resistance of $(Mn_{0.2}Co_{0.2}Ni_{0.2}Fe_{0.2}Ce_{0.2})_3O_4$@PPy composites. *Ceram. Int.* **2025**, *51*, 7026–7037.

[15] Liu, P. B.; He, Z. Z.; Li, X. C.; Ding, L. F.; Liu, S. H.; Kong, J. Multifunctional hollow carbon microspheres enable superior electromagnetic wave response and corrosion barrier. *Adv. Mater.* **2025**, *37*, 2500646.

[16] Rost, C. M.; Sachet, E.; Borman, T.; Moballegh, A.; Dickey, E. C.; Hou, D.; Jones, J. L.; Curtarolo, S.; Maria, J. P. Entropy-stabilized oxides. *Nat. Commun.* **2015**, *6*, 8485.

[17] Wang, W. L.; Sun, G. X.; Sun, X. N.; Zhang, Z. X.; Zhang, J. T.; Liang, Y. J.; Bi, J. Q. Electromagnetic wave absorbing properties of high-entropy transition metal carbides powders. *Mater. Res. Bull.* **2023**, *163*, 112212.

[18] Wen, Z. H.; Liu, Y. W.; Yang, J.; Chen, Y. H.; Fu, Y. M.; Zhuang, L.; Yu, H. L.; Chu, Y. H. Exceptional oxidation resistance of high-entropy carbides up to 3600 °C. *Adv. Mater.* **2025**, *37*, 2507254.

[19] Yang, W.; Shen, J. X.; Wang, Z. Y.; Ma, G. S.; Ke, P. L.; Wang, A. Y. Mechanical and electrochemical properties of $(MoNbTaTiZr)_{1-x}N_x$ high-entropy nitride coatings. *J. Mater. Sci. Technol.* **2025**, *208*, 78–91.

[20] Qiu, H. X.; Peng, S.; Zou, Y. S.; Cui, X. J.; Zhao, Y. H.; Wang, X. H.; Sun, D. E. Effect of nitrogen content on mechanical properties and microstructure of $(TiZrNbCrSi)N_x$ high-entropy nitride coating. *J. Alloys Compd.* **2025**, *1022*, 179822.

[21] Zhang, W. M.; Zhao, B.; Ni, N.; Xiang, H. M.; Dai, F. Z.; Wu, S. J.; Zhou, Y. C. High entropy rare earth hexaborides/tetraborides (HE REB_6/HE REB_4) composite powders with enhanced electromagnetic wave absorption performance. *J. Mater. Sci. Technol.* **2021**, *87*, 155–166.

[22] Wang, F. W.; Xu, L.; Zou, J.; Liu, J. J.; Liang, H. Y.; Ji, W.; Wang, W. M.; Fu, Z. Y. Pressureless densification and properties of high-entropy boride ceramics with B_4C additions. *J. Mater. Sci. Technol.*

2024, *190*, 1–9.

[23] Lei, B. S.; Zhou, C.; Zhang, K. N.; Li, J. W.; Miao, H. R.; Wang, H.; Fan, Q. K.; Yang, Z. M.; Wang, G.; Li, Y. et al. Plasma-induced geometry engineering in high-entropy oxide composites for superior electromagnetic absorption. *Adv. Funct. Mater.* **2025**, *35*, 2425262.

[24] Lei, B. S.; Wang, G.; Li, C. Y.; Fan, Q. K.; Yang, Z. M.; Li, Y.; Zhou, C.; Kong, C. C. Rapid synthesis and enhanced microwave absorption of carbon-supported high-entropy metal oxide. *J. Alloys Compd.* **2025**, *1010*, 176964.

[25] Hu, Y. J.; Sun, G. H.; Zhang, Q.; Li, M. L.; Zhu, J. P.; Shao, G.; Wang, H. L.; Xu, H. L.; Lu, H. X. High-entropy perovskite ceramics with excellent broadband wave-absorbing properties by one-step sintering. *Ceram. Int.* **2025**, *51*, 42756–42768.

[26] Yang, B. B.; Zhang, Y.; Pan, H.; Si, W. L.; Zhang, Q. H.; Shen, Z. H.; Yu, Y.; Lan, S.; Meng, F. Q.; Liu, Y. Q. et al. High-entropy enhanced capacitive energy storage. *Nat. Mater.* **2022**, *21*, 1074–1080.

[27] Anandkumar, M.; Kannan, P. K.; Sudarsan, S.; Uchaev, D. A.; Trofimov, E. A. Reusable high-entropy oxide environmental photocatalyst towards toxic Cr(VI) reduction with tailored bandgap via solution combustion synthesis. *Adv. Powder Technol.* **2024**, *35*, 104429.

[28] Du, B.; Liu, Y. R.; Xu, J. Y.; Ouyang, Y. M.; Cheng, Y.; Zhang, T. Fabrication and electromagnetic wave absorbing properties of the $(Hf_{0.25}Zr_{0.25}Nb_{0.25}Ta_{0.25})C$ high-entropy ceramics. *J. Alloys Compd.* **2023**, *969*, 172403.

[29] Gu, F. C.; Wang, W.; Meng, H.; Liu, Y. W.; Zhuang, L.; Yu, H. L.; Chu, Y. H. Lattice distortion boosted exceptional electromagnetic wave absorption in high-entropy diborides. *Matter* **2025**, *8*, 102004.

[30] Li, M. R.; Zhi, Q.; Li, J. L.; Wu, C. W.; Jiang, X. W.; Min, Z. Y.; Zhang, R.; Wang, H. L.; Wang, H. B.; Fan, B. B. $Sr(Cr_{0.2}Mn_{0.2}Fe_{0.2}Co_{0.2}Ni_{0.2})O_3$: A novel high-entropy perovskite oxide with enhanced electromagnetic wave absorption properties. *J. Materiomics* **2024**, *10*, 1176–1185.

[31] Zhou, L.; Hu, P. F.; Bai, M.; Leng, N.; Cai, B.; Peng, H. L.; Zhao, P. Y.; Guo, Y. Q.; He, M. K.; Wang, G. S. et al. Harnessing the electronic spin states of single atoms for precise electromagnetic modulation. *Adv. Mater.* **2025**, *37*, 2418321.

[32] Yuan, Y.; Jiang, J. H.; Wu, L. J.; Song, C. Y.; Lei, Y. H.; Zhang, F.; Fan, R. H. Multifunctional coatings based on high-entropy oxide composites in electromagnetic wave absorption and anti-corrosion properties. *Ceram. Int.* **2025**, *51*, 35119–35132.

[33] Hou, Y. L.; Liu, Z. Y.; Wang, Q.; Yu, Z.; Xing, R. Z.; Yu, Z. L.; Tang, Y. S.; Kong, J. Magnetic graphene composite aerogel for highly efficient electromagnetic wave absorption and anti-corrosion. *J. Mater. Sci. Technol.* **2026**, *251*, 1–10.

[34] Liao, Z. J.; Ma, M. L.; Tong, Z. Y.; Wang, R. Z.; Bi, Y. X.; Chen, Y.; Chung, K. L.; Ma, Y. Fabrication of $ZnFe_2O_4$/C@PPy composites with efficient electromagnetic wave absorption properties. *J. Colloid Interf. Sci.* **2021**, *602*, 602–611.

[35] Wang, D. S.; Yang, P. X.; Hu, Y. Z.; Cui, Z. Y.; Du, Z. L.; Yang, P. A.; Yi, S.; Rao, J. S.; Zhang, Y. X. 1D–3D biological template loaded NiCo nanowires at high temperatures as a broadband, lightweight electromagnetic wave absorbing material. *Powder Technol.* **2023**, *426*, 118670.

[36] Ren, S. Z.; Mo, P. P.; Shui, A. Z.; Qian, J. J.; Du, B. ZnCo-MOF derived porous ZnO/Co/C composites as superior electromagnetic wave absorbers. *J. Mater. Sci.: Mater. Electron.* **2024**, *35*, 530.

[37] Liu, C. C.; Zhu, T.; Jia, J.; Zhu, Y.; Chen, Q. Y.; Zhang, W.; Zhang, W. L.; Song, H.; Wang, Y. Z.; Jiang, N. Facile synthesis of novel nitrogen-doped diamond with excellent microwave absorption and thermal conductive performance. *Diam. Relat. Mater.* **2025**, *151*, 111789.

[38] Liu, P. J.; Ng, V. M. H.; Yao, Z. J.; Zhou, J. T.; Lei, Y. M.; Yang, Z. H.; Lv, H. L.; Kong, L. B. Facile synthesis and hierarchical assembly of flowerlike NiO structures with enhanced dielectric and microwave absorption properties. *ACS Appl. Mater. Interfaces* **2017**, *9*, 16404–16416.

[39] Qian, J. J.; Ma, D. D.; Du, B.; Shui, A. Z.; Wang, S. H.; Shan, Q. L.; Wang, Y. Q.; Chang, Q. B. High-performance electromagnetic wave absorbers based on hierarchically porous $(Zn_{1/2}Ni_{1/2})Co_2O_4$ spinel clusters. *J. Alloys Compd.* **2024**, *987*, 174189.

[40] Li, M. R.; Li, W.; Wang, Y. X.; Sun, F.; Wang, Q.; Tan, D. L.; Zhang, R.; Wang, H. L.; Shao, G.; Liu, Y. L. et al. Entropy-driven microwave absorption enhancement in hexagonal $(Ba_{1/3}Sr_{1/3}Ca_{1/3})FeO_3$ perovskite. *J. Adv. Ceram.* **2025**, *14*, 9221059.

[41] Dai, G. H.; Deng, R. X.; Zhang, T.; Yu, Y.; Song, L. X. Quantitative evaluation of loss capability for *in situ* conductive phase enhanced microwave absorption of high-entropy transition metal oxides. *Adv. Funct. Mater.* **2022**, *32*, 2205325.

[42] Yan, Z. K.; Li, D. P.; Zhang, X.; Men, Q. Q.; Fan, B. B.; Guan, L.; Guo, X. Q.; Zhang, R.; Zhao, B. Dual-phase high-entropy $(FeCoNiZn)_xV_2O_y$ oxides with promising microwave absorption properties. *Ceram. Int.* **2022**, *48*, 36871–36879.

[43] Ma, Y. Z.; Zhang, S. S.; Yang, X. F.; Wang, Q. Preparation and electromagnetic absorption properties of bulk (MgCoNiCuZn)O. *J. Electron. Mater.* **2023**, *52*, 6959–6967.

[44] Zhao, B.; Yan, Z. K.; Du, Y. Q.; Rao, L. J.; Chen, G. Y.; Wu, Y. Y.; Yang, L. T.; Zhang, J. C.; Wu, L. M.; Zhang, D. W. et al. High-entropy enhanced microwave attenuation in titanate perovskites. *Adv. Mater.* **2023**, *35*, 2210243.

[45] Liu, C. C.; Chen, Q. Y.; Sun, P.; Wang, X. Y.; Zeng, S. Y.; Chen, Q. J.; Zhu, T.; Zhu, Y.; Zhang, W. L.; Song, H. et al. Synthesis of novel high-entropy diborides with high-efficiency electromagnetic wave absorption and excellent thermal stability. *J. Adv. Ceram.* **2025**, *14*, 9221030.

[46] Zhang, W. M.; Zhao, B.; Xiang, H. M.; Dai, F. Z.; Wu, S. J.; Zhou, Y. C. One-step synthesis and electromagnetic absorption properties of high entropy rare earth hexaborides (HE REB_6) and high entropy rare earth hexaborides/borates (HE REB_6/HE $REBO_3$) composite powders. *J. Adv. Ceram.* **2021**, *10*, 62–77.

[47] Zhou, Y. C.; Zhao, B.; Chen, H.; Xiang, H. M.; Dai, F. Z.; Wu, S. J.; Xu, W. Electromagnetic wave absorbing properties of TMCs (TM = Ti, Zr, Hf, Nb and Ta) and high entropy $(Ti_{0.2}Zr_{0.2}Hf_{0.2}Nb_{0.2}Ta_{0.2})C$. *J. Mater. Sci. Technol.* **2021**, *74*, 105–118.

[48] Zhao, X.; Bai, Y. H.; Yang, Y.; Yao, Z. L.; Wu, Y. H.; Liu, J.; Ren, K.; He, J. B.; Du, H. L.; Song, Y. Ultrafast carbothermal shock synthesis of submicron high-entropy carbides: Dual enhancement of oxidation resistance and microwave absorption. *Mater. Des.* **2025**, *257*, 114436.

[49] Häcker, J.; Rommel, T.; Lange, P.; Kampmann, F.; Remmlinger, J.; Zhao-Karger, Z.; Friedrich, K. A.; Nojabaee, M. Interfacial processes of Mg anodes for magnesium-sulfur batteries: An EIS study. *J. Magnes. Alloys* **2025**, *13*, 2680–2698.

[50] Zamani, P.; Valefi, Z.; Jafarzadeh, K. Comprehensive study on corrosion protection properties of Al_2O_3, Cr_2O_3 and Al_2O_3–Cr_2O_3 ceramic coatings deposited by plasma spraying on carbon steel. *Ceram. Int.* **2022**, *48*, 1574–1588.